

INFLUENCE OF INFLOW TURBULENCE INTENSITY VARIATIONS IN AN AXIAL TURBINE USING 3D RANS COMPUTATIONS

Jesuino Takachi Tomita, jtakachi@ita.br

João Roberto Barbosa, barbosa@ita.br

Technological Institute of Aeronautics - ITA

Abstract. *The requirements for the flow leaving the combustion chamber to enter the turbine are tight to guarantee good turbine operation. Temperature and pressure radial and circumferential distributions, as prescribed at design, cannot vary much. Among the important parameters that influence significantly the turbine performance is the inflow level of turbulence intensity. In this work, a in-house developed CFD software is used to calculate the flow parameters in the turbine, a solution that involves the continuity, momentum and energy equations, together with a model for the turbulent stress terms. Different values of turbulence intensity were used for the study of the design 3D flow in the axial turbine. The Reynolds-Averaged Navier-Stokes and one-equation turbulence model were used for the calculations. The results are presented for each blade row inlet and outlet, along the blade span and show that until 5% of turbulence intensity, in the cases simulated, the influence on turbine mass-flow is slightly and the turbulent viscosity ratio distribution is quite different for each turbulence intensity value mainly for flow separation regions.*

Keywords: *turbomachines, CFD, turbulence, gas turbine, numerical methods.*

1. INTRODUCTION

The flow in turbomachines is recognized as one of the most complex in the field of fluid dynamics. Three-dimensional flowfield calculation in turbomachines is usually a complex and costly task. Because the components, compressor or turbine, have their particularities, different strategies are required to arrive at a converged and meaningful solution. A recent work (Denton, 1990) describe the difficulties to simulate high pressure compressor due to the "numerical surge" caused by the complexity for starting the CFD calculations due to the possibility of the blades operate near stall. The calculation may fail as a result of the transient induced by the initial guess rather than because of a genuinely unstable operating point.

Robust and accurate CFD codes are developed specially to solve specific problems (Adumitroaie *et al.*, 1998) and (Veullot, 1985). They must account for very different requirements like internal or external flows, incompressible or compressible, low or high Reynolds numbers, with or without chemical reactions and dissociations, porous-media, unsteady or steady-state, to name a few. Each case requires specific theoretical modeling, numerical formulations and computer implementation. Complex geometries and flows require great attention during the mesh generation, to provide the quantity and position of the nodes to assure caption of the flow particulars.

The study of the flowfield in turbomachines is nowadays vastly made with CFD, mainly when aiming at optimization of high performance components (Lapworth and Shahpar, 2004). For compressors and turbines some specific numerical treatments are necessary because two frames of reference must be used: rotating and non-rotating. A rotor row is treated within the rotating frame of reference and a stator row within the non-rotating (or stationary) frame of reference. A comparison of the use of the CFD codes for the flow calculation using these two different reference frames, based on absolute and relative velocities, can be found in open literature (Chen *et al.*, 1997).

Recently, Denton published an interesting work (Denton, 2010) about several numerical and modeling issues, which should be improved, and the limitations of CFD codes. Denton mentioned the importance of better understanding the details of all physical phenomena involved in the complex flowfield within turbomachines to select the numerical methods and to develop the computer code. It is very important to mention that, before studying the flowfield behavior in compressors and turbines, it is strongly advisable to understand the operation mechanisms and design issues of each component.

In this work, the authors compare the results of the numerical simulation of a single stage-axial flow turbine, for different turbine inlet turbulence intensity. The results were obtained using an in-house developed CFD code, written in FORTRAN 95 language (Tomita, 2009). The software is a three-dimensional CFD code able to solve the full Navier-Stokes equations, including turbulence effects. It was specially developed for the study of the flow in turbomachines. The code is also capable of solving other flows, internal and external, like in nozzles, around wings and aerospace configurations. The discretization used is cell-centered finite-volume, implemented for unstructured mesh. All details required for the study of turbomachines present in a gas turbine are incorporated.

Several turbulence models were tested for different engineering problems and in the case of turbomachinery flow calculation some of them were published including one and two equation turbulence models (Casey, 1984; Anderson

et al., 2003). The results of flowfield calculation using Reynolds Stress Model (RSM) were compared with two equation turbulence model results and the solution show that the standart k- ω SST model offers the best trade-off between accuracy and computational cost (Soghe *et al.*, 2010).

There is no general turbulence model, there is a good turbulence modeling depending on the problem to be solved (wall bounded flow, free-shear flow, aerodynamics, reactive flow, high separated flow and so on). The one-equation turbulence model developed by Spalart and Allmaras (Spalart and Allmaras, 1992) to use in aerodynamics flow calculation was chosen for this work, based on the recommendations of the literature associated to turbomachines including high performance transonic rotors (Grosvenor, 2007; Fidalgo *et al.*, 2010) and studies involving engine hot gas ingestion in military aircraft (Richardson *et al.*, 2006). The hybrid Large Eddy Simulation (LES) tool specifically developed for turbomachinery flows also use the one-equation turbulence model based on the modified eddy viscosity transport. Unsteady Reynolds-Averaged Navier-Stokes (RANS) solvers for high loading cascades with active control in the stator blades also show the applicability of the Spalart and Allmaras model (Gmelin *et al.*, 2010) for flow analysis involving secondary flow at walls due to the actuation system. Studies involving canned CFD software to calculate the flow in mainstream gas ingestion into inter-rows cavity also use the turbulence model above mentioned (Dunn *et al.*, 2010). Some turbulence models have been developed to study the flow transition point mainly for drag decreasing as nacelle, fuselage among others, but this is not the scope of present work.

The methodologies adopted for the design of the turbine is not the objective of this work. Instead, it is only mentioned that a meanline technique and a loss model was employed.

Accordingly, the flow in a single-stage axial flow turbine is calculated and the results and numerical issues are discussed.

2. Continuity, Momentum and Energy Equations

Using the Einstein notation, the equations are defined by

- Mass:

$$\frac{\partial \rho}{\partial t} + \frac{\partial}{\partial x_j}(\rho W_j) = 0, \quad (1)$$

- Momentum:

$$\frac{\partial}{\partial t}(\rho W_i) + \frac{\partial}{\partial x_j}(\rho W_i W_j) + \frac{\partial p}{\partial x_i} - \frac{\partial \tau_{ij}}{\partial x_j} + \Psi_i = 0, \quad (2)$$

- Energy:

$$\frac{\partial e}{\partial t} + \frac{\partial}{\partial x_j}[(e + p)W_j - \tau_{ij}W_i + q_j] = 0. \quad (3)$$

The fluid is considered newtonian and the viscous stresses are considered linear and proportional to the rate of strain, hence:

$$\tau_{ij} = \mu \left(\frac{\partial W_i}{\partial x_j} + \frac{\partial W_j}{\partial x_i} \right) + \lambda \delta_{i,j} \left(\frac{\partial W_k}{\partial x_k} \right), \quad (4)$$

where μ is the molecular dynamic viscosity and λ is the second coefficient of viscosity. Admitting the validity of the Stokes hypothesis, hence $\lambda = -2/3\mu$. Variable Ψ represents the terms related to the rotation of the fluid flow in the rotating channels (Coriolis and centrifugal forces), that is $\Psi^T = [0, \rho\omega^2x + 2\rho\omega W_y, \rho\omega^2y - 2\rho\omega W_x, 0, 0]$ and ω is the angular velocity.

Analyzing the magnitudes of the variables involved in the above equations it is seen that they differ by several order of magnitudes. Bearing in mind their numerical solution, it is possible to avoid the numerical errors related to those differences in numerical values by normalizing the variables.

$$\begin{aligned} \hat{\rho} &= \frac{\rho}{\rho_0}, & \hat{W}_i &= \frac{W_i}{a_0}, & \hat{\kappa} &= \frac{\kappa}{\kappa_0}, \\ \hat{x} &= \frac{x}{l_0}, & \hat{T} &= \frac{T}{T_0}, & \hat{t} &= t \frac{a_0}{l_0}, \\ \hat{y} &= \frac{y}{l_0}, & \hat{e} &= \frac{e}{\rho a_0^2}, & \hat{\lambda} &= \frac{\lambda}{\mu_0}, \\ \hat{z} &= \frac{z}{l_0}, & \hat{\mu} &= \frac{\mu}{\mu_0}, & \hat{P} &= \frac{P}{P_0}, \end{aligned}$$

where the Reynolds number is calculated by $Re_0 = \rho_0 a_0 l_0 / \mu_0$ for the internal flow computations and $Re_\infty = \rho_0 |\vec{W}| l_0 / \mu_0$ for the external. The Mach number is calculated by $M_\infty = |\vec{W}| / a_0$, where the subscripts 0 and ∞ mean referential properties from the stagnation conditions and freestream conditions, respectively. These new defined parameters are called

- l_0 = characteristic length,
- $\hat{\rho}$ = dimensionless density,
- \hat{x} = dimensionless coordinate of a specific point, the same rule is valid for y and z coordinates,
- \hat{W}_i = dimensionless velocity,
- \hat{T} = dimensionless temperature,
- \hat{e} = dimensionless total energy,
- $\hat{\mu}$ = dimensionless molecular dynamic viscosity,
- $\hat{\kappa}$ = dimensionless thermal conductivity,
- \hat{t} = dimensionless time,
- $\hat{\lambda}$ = dimensionless second viscosity coefficient,
- \hat{P} = dimensionless pressure,
- Re_0 = Reynolds number calculated using dimensionless variables.

Turbulence, as usually understood today, allows that the flow properties may be represented as the sum of the mean value of the property and a fluctuation of that property:

$$A = \bar{A} + A', \quad (5)$$

$$A = \tilde{A} + A'' \quad (6)$$

where the overbar and tilde stand for mean; the prime and double prime stand for fluctuation of the property A .

Among the different ways to extract the averages, in this work the Reynolds and Favre averages were selected. They are defined by, respectively,

$$\bar{A}_{Reynolds} = \lim_{T \rightarrow \infty} \frac{1}{T} \int_t^{t+T} A dt, \quad (7)$$

$$\tilde{A}_{Favre} = \frac{1}{\bar{\rho}} \lim_{T \rightarrow \infty} \frac{1}{T} \int_t^{t+T} \rho A dt, \quad (8)$$

where $\bar{\rho}$ is the Reynolds average of ρ (density) and T is a time interval.

The averaging procedures use the definitions

$$\begin{aligned} W_i &= \tilde{W}_i + W_i'', \\ H &= \tilde{H} + H'', \\ e &= \tilde{e} + e'', \\ T &= \tilde{T} + T'', \\ q_i &= \tilde{q}_i + q_i', \\ \rho &= \bar{\rho} + \rho', \\ p &= P + p', \end{aligned} \quad (9)$$

Applying the averages above indicated to the non-dimensionalized equations, the following equations were obtained:

$$\frac{\partial \bar{\rho}}{\partial t} + \frac{\partial}{\partial x_j} (\bar{\rho} \tilde{W}_j) = 0 \quad (10)$$

$$\frac{\partial}{\partial t} (\bar{\rho} \tilde{W}_i) + \frac{\partial}{\partial x_j} (\bar{\rho} \tilde{W}_i \tilde{W}_j) + \frac{\partial P}{\partial x_i} - \frac{\partial}{\partial x_j} (\bar{\tau}_{ij} - \overline{\rho W_i'' W_j''}) + \bar{\Psi}_i = 0 \quad (11)$$

$$\frac{\partial \bar{e}}{\partial t} + \frac{\partial}{\partial x_j} \left[(\bar{e} + P) \tilde{W}_j - \tilde{W}_i (\bar{\tau}_{ij} - \overline{\rho W_i'' W_j''}) - \overline{W_i'' (\tau_{ij} - \frac{\rho W_i'' W_j''}{2})} + \bar{q}_j + \overline{\rho W_j'' h} \right] = 0 \quad (12)$$

Equations 10, 11 and 12 are similar to equations 1, 2 and 3 except for the following terms associated with the turbulence, where:

- $\overline{\rho \hat{W}_i'' \hat{W}_j''}$: usually named Reynolds Stress Tensor (RST),
- $\frac{1}{2} \overline{\rho \hat{W}_i'' \hat{W}_i''}$: usually named kinetic energy of the (turbulent) fluctuations,
- $\overline{\rho \hat{W}_i'' h''}$: usually named molecular transport of heat.

After the non-dimensionalization and collection of the appropriate terms, it is possible to write this "turbulent" system of partial differential equations in matricial form

$$\frac{\partial \bar{Q}}{\partial t} + \frac{\partial \bar{E}}{\partial \hat{x}} + \frac{\partial \bar{F}}{\partial \hat{y}} + \frac{\partial \bar{G}}{\partial \hat{z}} + \bar{\Psi} = 0, \quad (13)$$

where Q is the vector of conserved variables, E , F and G the flux vectors and $\bar{\Psi}$ the source terms.

In equation 13 the over hat stands for non-dimensional variables and the overbar for the averages (RANS or Favre) as indicated by equations 7 and 8.

The flux vectors are decomposed of non-viscous, viscous and turbulent components, as indicated by equations 14, 15 and 16

$$E = E_e + E_v + E_t, \quad (14)$$

$$F = F_e + F_v + F_t, \quad (15)$$

$$G = G_e + G_v + G_t \quad (16)$$

The convective terms are represented by the subscript e . The viscous terms are represented by the subscript v . The components containing the fluctuations terms are represented by subscript t . The matricial representation of the terms are, therefore

$$\bar{Q} = \begin{Bmatrix} \bar{\rho} \\ \bar{\rho \hat{W}_x} \\ \bar{\rho \hat{W}_y} \\ \bar{\rho \hat{W}_z} \\ \bar{\hat{e}} \end{Bmatrix}, \quad \bar{E}_e = \begin{Bmatrix} \bar{\rho \hat{W}_x} \\ \bar{\rho \hat{W}_x \hat{W}_x} + P \\ \bar{\rho \hat{W}_x \hat{W}_y} \\ \bar{\rho \hat{W}_x \hat{W}_z} \\ (\bar{\hat{e}} + P) \bar{\hat{W}_x} \end{Bmatrix}, \quad \bar{F}_e = \begin{Bmatrix} \bar{\rho \hat{W}_y} \\ \bar{\rho \hat{W}_y \hat{W}_x} \\ \bar{\rho \hat{W}_y \hat{W}_y} + P \\ \bar{\rho \hat{W}_y \hat{W}_z} \\ (\bar{\hat{e}} + P) \bar{\hat{W}_y} \end{Bmatrix}, \quad \bar{G}_e = \begin{Bmatrix} \bar{\rho \hat{W}_z} \\ \bar{\rho \hat{W}_z \hat{W}_x} \\ \bar{\rho \hat{W}_z \hat{W}_y} \\ \bar{\rho \hat{W}_z \hat{W}_z} + P \\ (\bar{\hat{e}} + P) \bar{\hat{W}_z} \end{Bmatrix}, \quad (17)$$

$$\bar{E}_t = \begin{Bmatrix} 0 \\ \frac{\bar{\rho \hat{W}_x'' \hat{W}_x''} - \bar{\hat{\tau}_{xx}}}{(\bar{\hat{e}} + P) \bar{\hat{W}_x''} - \bar{\hat{\tau}_{xf}}} \\ \frac{\bar{\rho \hat{W}_x'' \hat{W}_y''} - \bar{\hat{\tau}_{yx}}}{(\bar{\hat{e}} + P) \bar{\hat{W}_x''} - \bar{\hat{\tau}_{xf}}} \\ \frac{\bar{\rho \hat{W}_x'' \hat{W}_z''} - \bar{\hat{\tau}_{zx}}}{(\bar{\hat{e}} + P) \bar{\hat{W}_x''} - \bar{\hat{\tau}_{xf}}} \\ (\bar{\hat{e}} + P) \bar{\hat{W}_x''} - \bar{\hat{\tau}_{xf}} \end{Bmatrix}, \quad \bar{F}_t = \begin{Bmatrix} 0 \\ \frac{\bar{\rho \hat{W}_y'' \hat{W}_x''} - \bar{\hat{\tau}_{yx}}}{(\bar{\hat{e}} + P) \bar{\hat{W}_y''} - \bar{\hat{\tau}_{yf}}} \\ \frac{\bar{\rho \hat{W}_y'' \hat{W}_y''} - \bar{\hat{\tau}_{yy}}}{(\bar{\hat{e}} + P) \bar{\hat{W}_y''} - \bar{\hat{\tau}_{yf}}} \\ \frac{\bar{\rho \hat{W}_y'' \hat{W}_z''} - \bar{\hat{\tau}_{zy}}}{(\bar{\hat{e}} + P) \bar{\hat{W}_y''} - \bar{\hat{\tau}_{yf}}} \\ (\bar{\hat{e}} + P) \bar{\hat{W}_y''} - \bar{\hat{\tau}_{yf}} \end{Bmatrix}, \quad \bar{G}_t = \begin{Bmatrix} 0 \\ \frac{\bar{\rho \hat{W}_z'' \hat{W}_x''} - \bar{\hat{\tau}_{zx}}}{(\bar{\hat{e}} + P) \bar{\hat{W}_z''} - \bar{\hat{\tau}_{zf}}} \\ \frac{\bar{\rho \hat{W}_z'' \hat{W}_y''} - \bar{\hat{\tau}_{yz}}}{(\bar{\hat{e}} + P) \bar{\hat{W}_z''} - \bar{\hat{\tau}_{zf}}} \\ \frac{\bar{\rho \hat{W}_z'' \hat{W}_z''} - \bar{\hat{\tau}_{zz}}}{(\bar{\hat{e}} + P) \bar{\hat{W}_z''} - \bar{\hat{\tau}_{zf}}} \\ (\bar{\hat{e}} + P) \bar{\hat{W}_z''} - \bar{\hat{\tau}_{zf}} \end{Bmatrix}, \quad (18)$$

$$\bar{E}_v = \frac{1}{Re_0} \begin{Bmatrix} 0 \\ \frac{\bar{\hat{\tau}_{xx}}}{\bar{\hat{\tau}_{xx} \bar{\hat{W}_x} + \bar{\hat{\tau}_{yx} \bar{\hat{W}_y} + \bar{\hat{\tau}_{zx} \bar{\hat{W}_z} + \gamma \left(\frac{\bar{\mu}_t}{Pr_t} + \frac{\bar{\mu}_t}{Pr_t} \right) \frac{\partial \bar{\hat{e}}_i}{\partial \hat{x}}}} \\ \frac{\bar{\hat{\tau}_{yx}}}{\bar{\hat{\tau}_{xx} \bar{\hat{W}_x} + \bar{\hat{\tau}_{yx} \bar{\hat{W}_y} + \bar{\hat{\tau}_{zx} \bar{\hat{W}_z} + \gamma \left(\frac{\bar{\mu}_t}{Pr_t} + \frac{\bar{\mu}_t}{Pr_t} \right) \frac{\partial \bar{\hat{e}}_i}{\partial \hat{x}}}} \\ \frac{\bar{\hat{\tau}_{zx}}}{\bar{\hat{\tau}_{xx} \bar{\hat{W}_x} + \bar{\hat{\tau}_{yx} \bar{\hat{W}_y} + \bar{\hat{\tau}_{zx} \bar{\hat{W}_z} + \gamma \left(\frac{\bar{\mu}_t}{Pr_t} + \frac{\bar{\mu}_t}{Pr_t} \right) \frac{\partial \bar{\hat{e}}_i}{\partial \hat{x}}}} \end{Bmatrix}, \quad (19)$$

$$\bar{F}_v = \frac{1}{Re_0} \begin{Bmatrix} 0 \\ \frac{\bar{\hat{\tau}_{yx}}}{\bar{\hat{\tau}_{yy} \bar{\hat{W}_y} + \bar{\hat{\tau}_{yx} \bar{\hat{W}_x} + \bar{\hat{\tau}_{yz} \bar{\hat{W}_z} + \gamma \left(\frac{\bar{\mu}_t}{Pr_t} + \frac{\bar{\mu}_t}{Pr_t} \right) \frac{\partial \bar{\hat{e}}_i}{\partial \hat{y}}}} \\ \frac{\bar{\hat{\tau}_{yy}}}{\bar{\hat{\tau}_{yy} \bar{\hat{W}_y} + \bar{\hat{\tau}_{yx} \bar{\hat{W}_x} + \bar{\hat{\tau}_{yz} \bar{\hat{W}_z} + \gamma \left(\frac{\bar{\mu}_t}{Pr_t} + \frac{\bar{\mu}_t}{Pr_t} \right) \frac{\partial \bar{\hat{e}}_i}{\partial \hat{y}}}} \\ \frac{\bar{\hat{\tau}_{zy}}}{\bar{\hat{\tau}_{yy} \bar{\hat{W}_y} + \bar{\hat{\tau}_{yx} \bar{\hat{W}_x} + \bar{\hat{\tau}_{yz} \bar{\hat{W}_z} + \gamma \left(\frac{\bar{\mu}_t}{Pr_t} + \frac{\bar{\mu}_t}{Pr_t} \right) \frac{\partial \bar{\hat{e}}_i}{\partial \hat{y}}}} \end{Bmatrix}, \quad (20)$$

$$\bar{G}_v = \frac{1}{Re_0} \begin{Bmatrix} 0 \\ \frac{\bar{\hat{\tau}_{zx}}}{\bar{\hat{\tau}_{zz} \bar{\hat{W}_z} + \bar{\hat{\tau}_{zx} \bar{\hat{W}_x} + \bar{\hat{\tau}_{zy} \bar{\hat{W}_y} + \gamma \left(\frac{\bar{\mu}_t}{Pr_t} + \frac{\bar{\mu}_t}{Pr_t} \right) \frac{\partial \bar{\hat{e}}_i}{\partial \hat{z}}}} \\ \frac{\bar{\hat{\tau}_{zy}}}{\bar{\hat{\tau}_{zz} \bar{\hat{W}_z} + \bar{\hat{\tau}_{zx} \bar{\hat{W}_x} + \bar{\hat{\tau}_{zy} \bar{\hat{W}_y} + \gamma \left(\frac{\bar{\mu}_t}{Pr_t} + \frac{\bar{\mu}_t}{Pr_t} \right) \frac{\partial \bar{\hat{e}}_i}{\partial \hat{z}}}} \\ \frac{\bar{\hat{\tau}_{zz}}}{\bar{\hat{\tau}_{zz} \bar{\hat{W}_z} + \bar{\hat{\tau}_{zx} \bar{\hat{W}_x} + \bar{\hat{\tau}_{zy} \bar{\hat{W}_y} + \gamma \left(\frac{\bar{\mu}_t}{Pr_t} + \frac{\bar{\mu}_t}{Pr_t} \right) \frac{\partial \bar{\hat{e}}_i}{\partial \hat{z}}}} \end{Bmatrix}, \quad (21)$$

The variables that have already appeared have the same meaning (but non-dimensionalized). During the non-dimensionalization and averaging of the variables, other definition came out:

$$\mu = \mu_l + \mu_t, \quad (22)$$

where μ is the effective coefficient of viscosity, μ_l is the molecular coefficient of viscosity, μ_t is the turbulent coefficient of viscosity, Pr_l is the laminar Prandtl number, Pr_t is the turbulent Prandtl number, assumed here equal to 0.9, γ is the ratio of specific heats and all terms containing fluctuation are calculated using turbulence modeling.

3. The One-Equation Spalart and Allmaras Turbulence Model

The model is valid for aerodynamics problems with high Reynolds number. It is an equation developed for the eddy viscosity transport $\tilde{\nu}$. For the sake of space only the specific treatment of the model will be described. All details, constants values and the development of all terms and its calibration are presented in (Spalart and Allmaras, 1992). The non-dimensional form of Spalart and Allmaras turbulence model is:

$$\begin{aligned} \frac{D\hat{\nu}}{Dt} = & c_{b1}[1 - f_{t2}]\hat{S}\hat{\nu} + \frac{1}{\sigma} \left[\nabla \cdot ((\hat{\nu} + \hat{\nu})\nabla\hat{\nu}) + c_{b2}(\nabla\hat{\nu})^2 \right] \frac{1}{Re_0} + \\ & - [c_{w1}f_w - \frac{c_{b1}}{\kappa^2}f_{t2}] \left[\frac{\hat{\nu}}{\hat{d}} \right]^2 \frac{1}{Re_0} + f_{t1}\delta U^2 Re_0 \end{aligned} \quad (23)$$

where

$$\hat{\nu} = \frac{\nu}{\mu_0/\rho_0}, \quad \hat{S} = \hat{S} + \frac{\hat{\nu}}{\kappa^2 \hat{d}^2} f_{v2} \frac{1}{Re_0}, \quad \hat{r} = \frac{\hat{\nu}}{\hat{S} K^2 \hat{d}^2} \frac{1}{Re_0}. \quad (24)$$

All other variables are dimensionless by definition. Applying the definition of material derivative

$$\frac{D(\)}{Dt} = \frac{\partial(\)}{\partial t} + \vec{W} \cdot \nabla(\), \quad (25)$$

and assuming that on the near wall region the velocity is small, the density variation can be neglected. The non-conservative form of Eq. 23 becomes

$$\begin{aligned} \frac{\partial\hat{\nu}}{\partial t} = & c_{b1}[1 - f_{t2}]\hat{S}\hat{\nu} + \frac{1}{\sigma} \left[\nabla \cdot ((\hat{\nu} + \hat{\nu})\nabla\hat{\nu}) + c_{b2}(\nabla\hat{\nu})^2 \right] \frac{1}{Re_0} + \\ & - [c_{w1}f_w - \frac{c_{b1}}{\kappa^2}f_{t2}] \left[\frac{\hat{\nu}}{\hat{d}} \right]^2 \frac{1}{Re_0} - \nabla \cdot (\hat{\nu}\vec{W}) + f_{t1}\Delta U^2 Re_0. \end{aligned} \quad (26)$$

The identity $\vec{W} \cdot \nabla(\hat{\nu}) = \nabla \cdot (\vec{W}\hat{\nu}) - \hat{\nu} \cdot \nabla\vec{W}$ was used to obtain Eq. 26.

In the equations above, subscript t stands for transition points, so that the corresponding terms are set to zero outside the transition region.

The Spalart and Allmaras turbulence model can be written in the following form:

$$\frac{\partial\hat{\nu}}{\partial t} = C(\hat{\nu}) + D(\hat{\nu}) + Prod(\hat{\nu}) + Dest(\hat{\nu}) + T, \quad (27)$$

where the convection term is

$$C(\hat{\nu}) = -\nabla \cdot (\hat{\nu}\vec{W}), \quad (28)$$

the diffusion term is

$$D(\hat{\nu}) = \frac{1}{\sigma} \left[\nabla \cdot ((\hat{\nu} + \hat{\nu})\nabla\hat{\nu}) + c_{b2}(\nabla\hat{\nu})^2 \right], \quad (29)$$

the production term is

$$Prod(\hat{\nu}) = c_{b1}[1 - f_{t2}]\hat{S}\hat{\nu}, \quad (30)$$

the destruction term is

$$Dest(\hat{\nu}) = \left[c_{w1}f_w - \frac{c_{b1}}{\kappa^2}f_{t2} \right] \left[\frac{\hat{\nu}}{\hat{d}} \right]^2, \quad (31)$$

and the transition term is

$$T = f_{t1}\Delta U^2. \quad (32)$$

4. The Second-Order Centered Spatial Discretization of Convective Terms

The centered discretization (Jameson *et al.*, 1981) of flux balance for each i -th control volume is based on information from the current volume and its neighbors. The flux is calculated by summation of the fluxes at all faces of the i -th control volume. The vectors E , F and G are divided in two terms, one for the convective and other for the viscous terms,

$$CONV(Q_i) = \sum_{k=1}^{n_{faces}} (E_e(Q_k)\vec{i} + F_e(Q_k)\vec{j} + G_e(Q_k)\vec{k}) \cdot \vec{S}_k. \quad (33)$$

The discretization is based on the arithmetical averages in a current i -th control volume and its neighbors nei at k -th face. The fluxes for each face can be written as

$$CONV(Q_k) = \frac{1}{2}(Q_k + Q_{nei}) \cdot \vec{S}_k, \quad (34)$$

where nei stands for the neighbor volume. The vectors E , F and G are written as functions of the vector of conserved variables Q .

The non-linear artificial dissipation model used in this work is a blend of second and fourth differences. The difference between the linear and the non-linear model is that the latter is dependent on the local pressure gradient. For regions with severe pressure gradients, this requires treatment and formulation different from other regions of potential flow. Two modified procedures have been implemented.

The first is based on the work of Jameson (Jameson *et al.*, 1981). Considering the directions in the computational coordinates i , j and k for i -th control volume,

$$DISS(Q_i) = DISS(Q_i)_i + DISS(Q_i)_j + DISS(Q_i)_k. \quad (35)$$

For each direction of i -th control volume, the neighbors $i-1$, $i+1$ for i direction, $j-1$, $j+1$ for j direction and $k-1$, $k+1$ for k direction are used for the calculations:

$$DISS(Q_i)_i = DISS(Q_i)_{i+1} - DISS(Q_i)_{i-1}, \quad (36)$$

$$DISS(Q_i)_j = DISS(Q_i)_{j+1} - DISS(Q_i)_{j-1}, \quad (37)$$

$$DISS(Q_i)_k = DISS(Q_i)_{k+1} - DISS(Q_i)_{k-1}. \quad (38)$$

Hence, $DISS(Q_i)_{i+1}$ is calculated by

$$DISS(Q_i)_{i+1} = \frac{(V_i)_{i+1}}{\Delta t} \left[\varepsilon_{i+1}^{(2)} ((Q_i)_{i+1} - (Q_i)_i - \varepsilon_{i+1}^{(4)} ((Q_i)_{i+2} - 3(Q_i)_{i+1} + 3(Q_i)_i - (Q_i)_i)) \right], \quad (39)$$

where, V_i is the volume of the i -th control volume. The coefficients $\varepsilon^{(2)}$ and $\varepsilon^{(4)}$ depend on the flow behavior, and are calculated using a pressure sensor. For the direction i

$$\varepsilon_{i+1}^{(2)} = k^{(2)} \max[(\zeta_i)_{i+1}, (\zeta_i)_i], \quad (40)$$

$$\varepsilon_{i+1}^{(4)} = \max[0, (k^{(4)} - \varepsilon_{i+1}^{(2)})], \quad (41)$$

where

$$(\zeta_i)_i = \frac{|p_{i+1} - 2p_i + p_{i-1}|}{|p_{i+1}| + 2|p_i| + |p_{i-1}|}. \quad (42)$$

The constants $k^{(2)}$ and $k^{(4)}$ assume the values $k^{(2)} = 1/4$ and $k^{(4)} = 1/256$. The term $\varepsilon^{(2)}$ is second-order accurate and the term $\varepsilon^{(4)}$ first-order. In regions with high gradients, the term $\varepsilon^{(2)}$ reduces the accuracy to first-order and the term $\varepsilon^{(4)}$, with fourth differences, tend to induce overshoots during the numerical iterations, being turned-off.

A second non-linear artificial dissipation model based on the reference (Mavriplis, 1990) was extended to three-dimensional space. In this model the artificial dissipation terms are divided by one undivided first-order accurate Laplacian operator, used only in the regions with strong gradients to avoid numerical oscillations, and one undivided third-order accurate biharmonic operator:

$$DISS(Q_i) = DISS(Q_i)_{Laplacian} + DISS(Q_i)_{biharmonic}. \quad (43)$$

Calculation starts with

$$D(Q_i) = \sum_{m=1}^{n_{neigh}} (Q_m - Q_i), \quad (44)$$

where, $nneigh$ is the number of neighbors of $i - th$ control volume. The biharmonic operator is calculated by:

$$DISS(Q_i)_{biharmonic} = \varepsilon^{(2)} \sum_{m=1}^{nneigh} [D(Q_m) - D(Q_i)] \left(\frac{A_m - A_i}{2} \right), \quad (45)$$

with

$$A_i = \sum_{k=1}^{nfaces} [(W_x)_k \vec{S}_k + (W_y)_k \vec{S}_k + (W_z)_k \vec{S}_k] + a_k Area_k, \quad (46)$$

where a_k is the speed of sound, based on the mean values at $i - th$ control volume and its neighbor at face k ; $Area_k$ is the area at face k belonging to the $i - th$ control volume and its neighbor.

The Laplacian operator is calculated replacing the quantities $D(Q_m)$ and $D(Q_i)$ in Eq. 45 by the quantities Q_m and Q_i and replacing the constant $\varepsilon^{(2)}$ by $\varepsilon^{(1)}$:

$$DISS(Q_i)_{Laplacian} = \varepsilon^{(1)} \sum_{m=1}^{nneigh} [Q_m - Q_i] \left(\frac{A_m - A_i}{2} \right). \quad (47)$$

The value of $\varepsilon^{(1)}$ is calculated using the pressure sensor

$$\varepsilon^{(1)} = \frac{\left| \sum_{k=1}^{nfaces} (p_k - p_i) \right|}{\sum_{k=1}^{nfaces} (p_k - p_i)}. \quad (48)$$

For this model, typical values are $\varepsilon^{(2)} = 1/2$ and $1/256 \leq \varepsilon^{(4)} \leq 3/256$, as indicated by Mavriplis (Mavriplis, 1990). The values used in this work are: $\varepsilon^{(2)} = 1/2$ and $\varepsilon^{(4)} = 3/256$.

The artificial dissipation scheme used in this work use the formulation of the first non-linear model presented, but replacing the term $V_i/\Delta t$ in Eq. 39 by the term $(A_m - A_i)/2$ calculated in Eq. 46. During the development of the CFD code, this modification resulted in a less dissipative behavior and provided a conservative dissipation using the averages given by the terms A_m and A_i .

5. Mesh Generation

The unstructured mesh is based on hexahedral elements. The code was developed to support unstructured mesh to improve the capability to add new features for complex geometries. A mesh of 523,422 nodes was used with the CFD solver. The mesh size was a result of the mesh dependence study and the requirements of the y^+ requirements for the turbulence model.

Firstly, with the design geometric parameters calculated, the corresponding solid was generated in a CAD software, from which the mesh was generated using the ICEM-CFD software and the nodes coordinates determined using another specially develop interpreter. In the sequence, the control volume properties were obtained (element volume, element face area, normal outward vectors, connectivity table, boundary and ghost elements, etc). The corresponding 3D view of the axial turbine is shown in Fig. 1 including the details of the mesh at the turbine rotor casing. The turbine tip speed is 380 m/s.



Figure 1. 3D view and the mesh at rotor casing of the single-stage axial-flow turbine

Seven control volumes were placed across the tip clearance. The nodes near the blade tip and near the casing are $5 \cdot 10^{-5}m$ apart from the walls. This value was forced with basis on estimates for a flat-plate y^+ .

6. Boundary Conditions and Numerical Issues

The boundary conditions were set at turbine inlet (stagnation properties); turbine outlet (static pressure with radial equilibrium from hub to tip); periodic conditions at mid-channel; and circumferentially averaged conserved variables mixing-plane at a positions enclosing the rotor. For subsonic flows, non-reflecting condition was implemented at inlet and outlet boundaries, based on the work of (Holmes, 1989), which uses the outgoing Riemann invariant methodology.

The viscous terms were discretized with a centered scheme and are computed only in the first step of time-integration procedure. The convective terms are computed for all time-integration steps and the artificial dissipation or the limiter functions are computed in alternate stages to save time.

For explicit time-marching, the time-integration of the turbulence equation is included in the Runge-Kutta steps, coupled to the continuity, momentum and energy equations. To avoid numerical instabilities and small Courant number based on CFL stability condition, the convection term of turbulence model was calculated implicitly as follows: all terms are calculated at the time n except the turbulence model convective term that is calculated at the time $n + 1$ using the Euler scheme.

This procedure run very well compared with a full explicit scheme for turbulent flows calculation. Although the Thomas algorithm can be directly used with structured grid, because it is possible to know the location of the zeros out of the dominant diagonal (tridiagonal, pentadiagonal or hexadiagonal), in unstructured mesh, the Thomas algorithm cannot be used directly, because the locations of the non-zeroes are unknown, resulting in a sparse matrix. In order to take advantage of the large number of zeroes in the matrix, it is also required special storage algorithms. In this work, the conjugated gradient is used.

The turbulence model was computed at every 3 Runge-Kutta iterations (this number can be set by the user). All transition terms are turned-off and the flow is considered completely turbulent.

The fluid model implemented in the CFD code considers the fluid as semi-perfect gas, with specific heats (c_p) and (c_v) varying with temperature. Hence, the specific heat ratio, the laminar Prandtl number and thermal conductivity are vary with temperature, requiring calculation for every control volume.

For turbulent flow simulations it is necessary to supply to the CFD solver the value of ν_T at boundary. For external flow ν_T must be given at farfield. For internal flow ν_T must be given at inlet. The Spalart and Allmaras turbulence model calculates the variable $\tilde{\nu}$ presented in Equation 26. The turbulent kinematic viscosity coefficient is used to calculate the turbulent dynamic viscosity coefficient necessary to calculate the terms of energy equation. For initial condition the value of $\tilde{\nu}$ can be estimated by $\nu/10$. Other option is to estimate the $\tilde{\nu}$ value using the turbulence intensity.

$$\tilde{\nu} = \sqrt{\frac{3}{2}} \vec{W} I l, \quad (49)$$

where I is the turbulent intensity and l is the turbulent length scale. The turbulent intensity can be estimated by the user or calculated using the following equation

$$I = 0.16 (Re)_{DH}^{-1/8}, \quad (50)$$

where the Reynolds number is calculated based on the hydraulic diameter defined by

$$D_H = \frac{D_t^2 - D_h^2}{D_t + D_h}, \quad (51)$$

where D_T is the tip diameter and D_H is the hub diameter. In the case of turboamachinery, this values are know from the design. The length scale can be estimated by

$$l = 0.07 D_H, \quad (52)$$

for fully-developed duct flow. In the case of wall-bounded flows

$$I = 0.4 \delta_{99}, \quad (53)$$

where δ_{99} is the boundary-layer thickness.

For turbulent flow simulations the viscous sublayer has to be resolved in an appropriate way to represent the physics correctly. It is required to have at least one mesh point inside the laminar sublayer. To calculate the distance between the first node on the wall and wall surface (y_p), the assumption of flat-plate turbulent flow is made. Equation 54 present the formulation used to calculate the y_p value based on y^+ ,

$$y^+ = \frac{\rho u_\tau y_p}{\mu}, \quad (54)$$

where u_τ is the skin friction velocity and it is calculated with

$$u_\tau = \sqrt{\frac{\tau_w}{\rho}}, \quad (55)$$

and

$$\tau_w = \frac{0.037W_\infty^2}{(Re)_\infty^{1/5}} \tag{56}$$

7. Results from CFD Simulations

The numerical iterations were monitored by means of the decayment of the residue of the conserved variables as shown in Fig. 2. The Courant number was increased in two steps (0.10, 0.12 and 0.17) as shown by the overshoots (5000 and 7000 iterations) in Fig. 2.

Table 1 shows the results of mass-flow and pressure ratio for each turbulence intensity value. Note that, the pressure ratio obtained from CFD calculations is different of design data obtained from meanline calculations using empirical loss models. The results from CFD solver show that the blade geometry should be changed to avoid high internal losses. Strictly speaking, the turbomachinery preliminary design based on meanline loss models is not capable to show all flow details due to the one-dimensional characteristic.

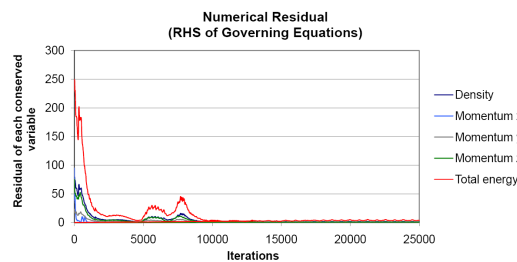


Figure 2. Monitoring of continuity, momentum and energy equations

Table 1. Comparison between mass-flow and pressure ratio

Description	Design Data	I = 0.5%	I = 1.0%	I = 1.5%	I = 2.0%	I = 2.5%	I = 5.0%
Mass-flow [kg/s]	19.83	20.27	20.50	20.33	20.34	20.51	20.23
Pressure ratio	1.83	1.66	1.67	1.67	1.67	1.67	1.67

Highly separated flow at rotor blade suction side will certainly decrease the pressure ratio across the turbine. Figure 3 shows the streamlines associated to the secondary flow in the rotor blade, where the flow properties were mass-averaged.

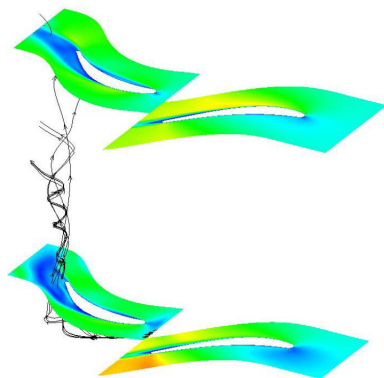


Figure 3. Streamlines of secondary flow

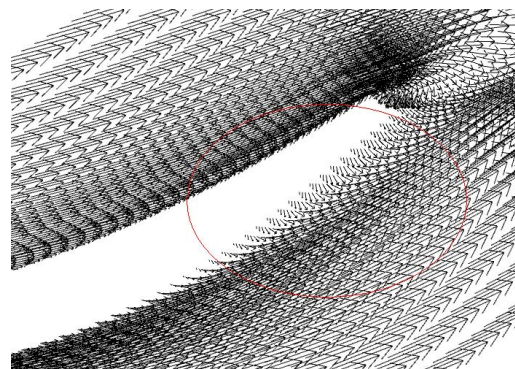


Figure 4. Reverse flow at NGV trailing edge

The Figs. 5 and 6 show the Mach number spanwise distribution for each turbulence intensity value. Note that, for NGV row all results are presented in the inertial reference frame (absolute values) and for rotor row in the non-inertial referencial frame (relative values). The influence of turbulence intensity on the Mach number distribution along the NGV is small, but in the rotor, where there is strong flow separation, the Mach number distribution is slightly different.

Figures 7 and 8 show the spanwise total pressure distribution for each turbulence intensity value. From the total pressure analysis it is possible to observe high differences in its distribution in the region close to the NGV trailing edge. At this region there is a reverse flow as shown in Fig. 4. The development of secondary flow in the rotor trailing edge region, from hub to tip, causes problems in the total pressure distribution. It is possible to observe that in the rotor trailing

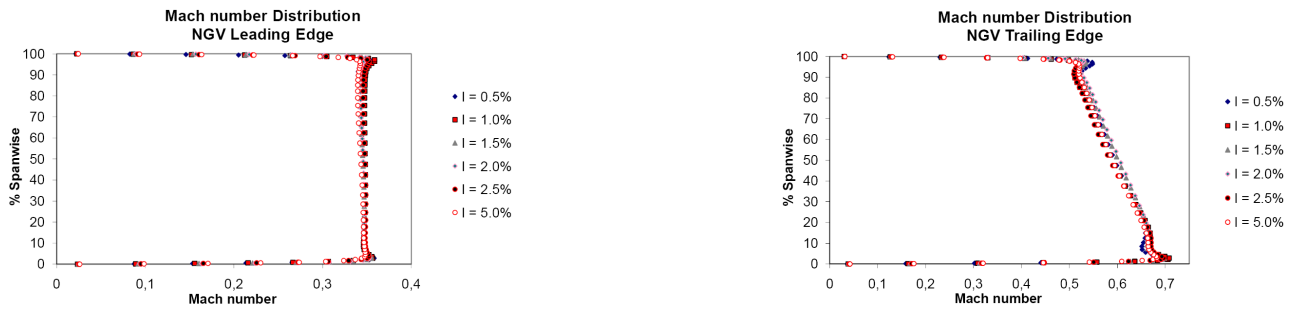


Figure 5. Mach number distribution at NGV blade row

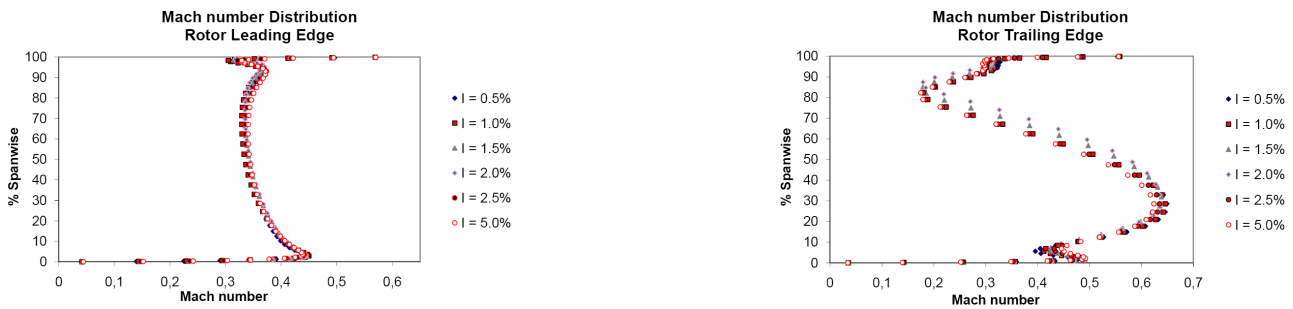


Figure 6. Mach number distribution at rotor blade row

edge there is a slightly difference between the total pressure distribution for each turbulence intensity value after 50% of rotor blade span.

The distribution of the velocity magnitude is shown in Figs. 9 and 10. The existence of high secondary flow at the rotor trailing edge causes large velocity spanwise variation. Note that the velocity in the rotor tip clearance is not zero because the velocity magnitude presented is the relative velocity and the boundary condition applied at the rotor casing considers this surface as a fixed frame of reference. These velocity distribution is undesirable due to the high variation (100 m/s - 350 m/s) from hub to tip. In the case of turbojet engine certainly these velocity profiles will affect the thrust. The effect of turbulence intensity only displaced upward the velocity profiles.

High differences of the viscosity ratio (ratio of turbulent flow eddy viscosity and fluid laminar viscosity) for inlet and outlet of each blade row can be observed in Figs. 11 and 12. In the rotor trailing edge, there are large spanwise differences of the viscosity ratio due to the high influence of secondary and tip clearance flows. These figures show clearly the magnitude of the viscosity ratio for different turbulence intensity.

Certainly, the tip clearance has a strong influence on turbulent flow in this region, what justifies the need to study the tip leakage flow and its associated losses. Tip clearance loss is one of the most serious topics to be explored by the turbine designer. The minimum gap is limited by manufacturing constraints and blade strain due to the thermal load and aeroelasticity. High tip clearance will produce high secondary flow and consequently the losses will increase and the turbine power output will decrease.

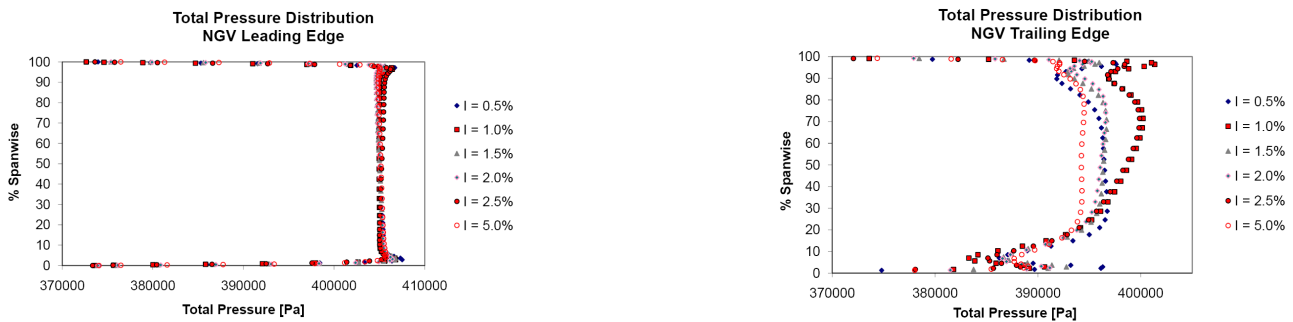


Figure 7. Total pressure distribution at NGV blade row

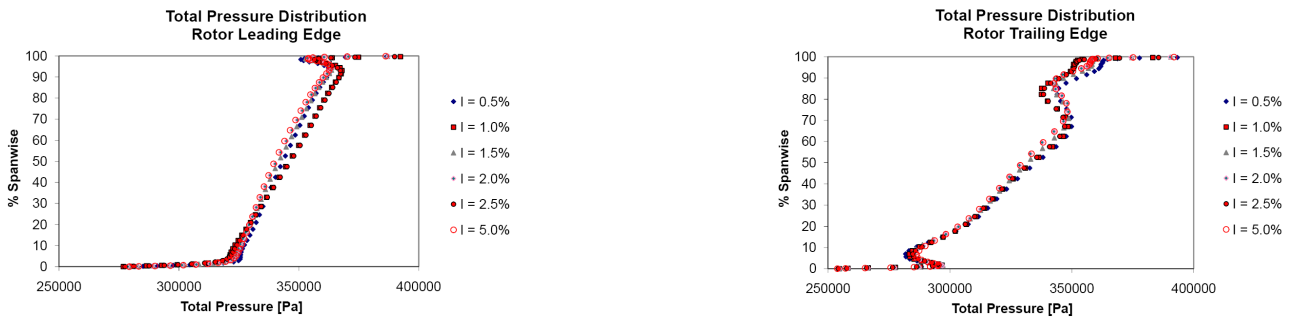


Figure 8. Total pressure distribution at rotor blade row

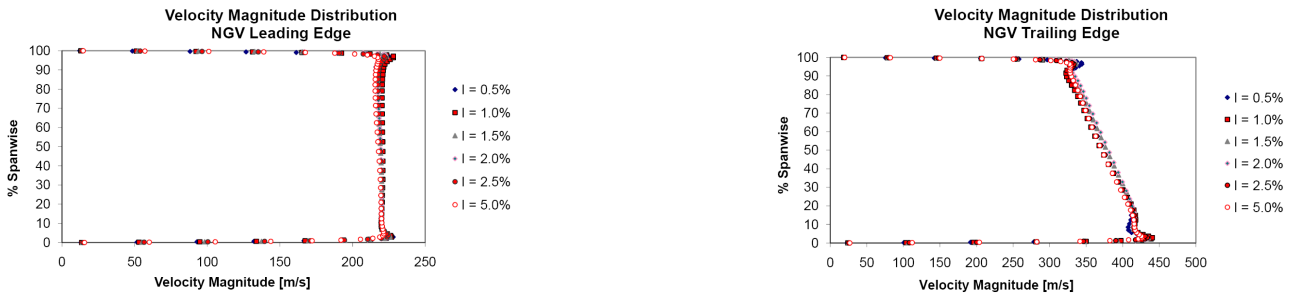


Figure 9. Velocity magnitude distribution at NGV blade row

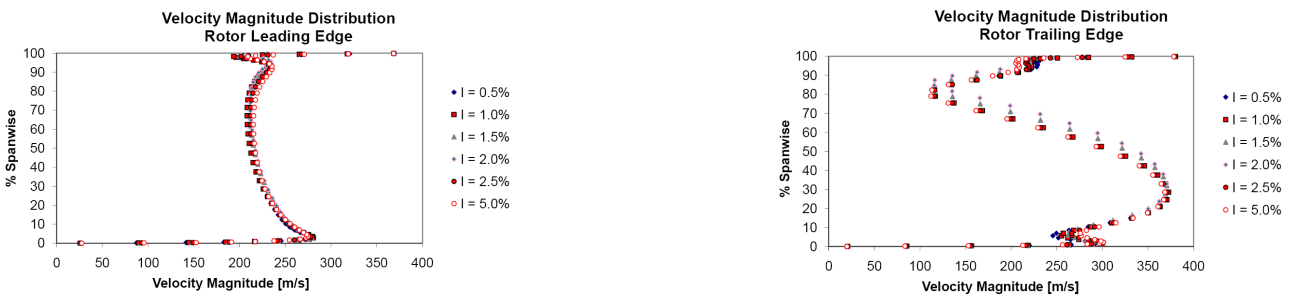


Figure 10. Velocity magnitude distribution at rotor blade row

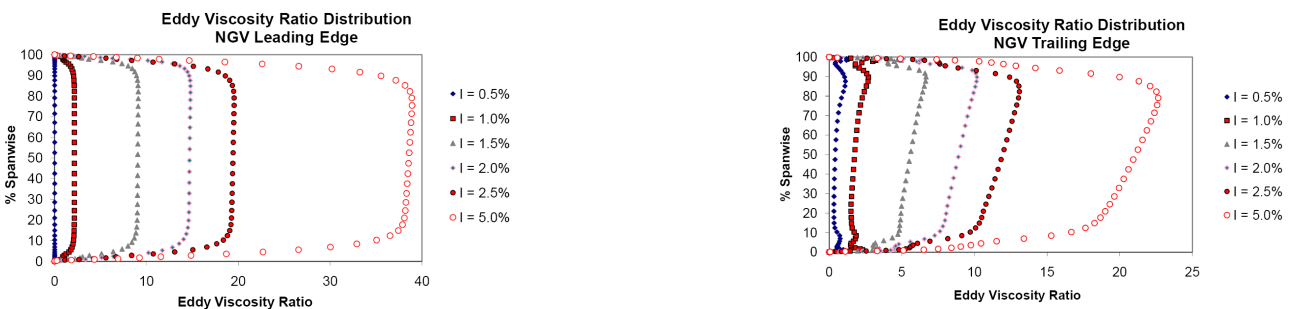


Figure 11. Viscosity ratio distribution at NGV blade row

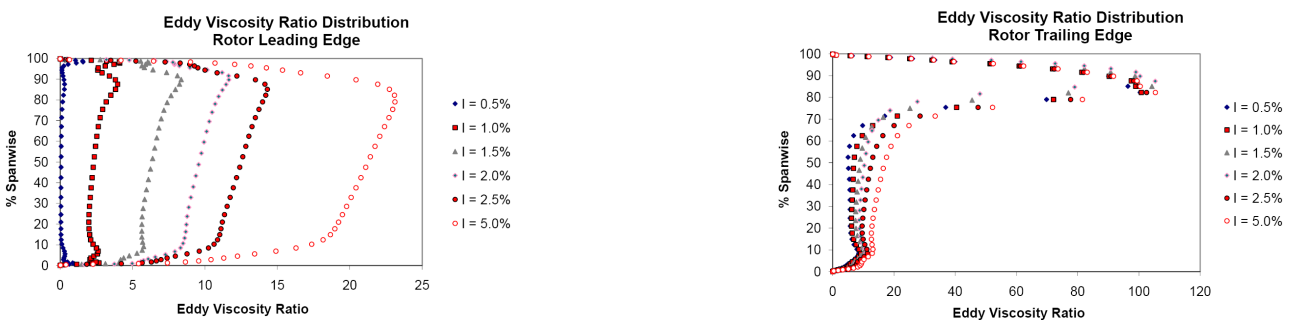


Figure 12. Viscosity ratio distribution at rotor blade row

8. Discussion and Conclusion

The 3D CFD code was capable to calculate the turbulent flow inside an axial flow turbine and some interesting results can be observed:

- The influence of turbulent intensity in the mass-flow and pressure ratio is less strong in the range of 0.5% - 5.0%;
- For high separation flow regions, the viscosity ratio distribution is quite different for different values of turbulence intensity;
- The viscosity ratio tends to be more aggressive near the rotor tip region due to the spanwise variation of the peripheral blade velocity;
- The tip clearance has high influence on secondary flow at the tip region, therefore requiring careful determined during the design process;
- A more accurate study should be made to analyse the local and global drag coefficient at blade surfaces to better understanding the effect of turbulence intensity;
- The turbulence intensity values used in this work are conservative in the sense of design procedure (design-point calculation), but this values are dependent on the quality of the gas distribution delivered from combustion chamber;

The CFD mass-flow and pressure ratio calculation are in good agreement with the design-point values used for the turbine design, but differences can be observed for pressure ratios. This may be due to the preliminary design tool, which is not capable to determine some flow characteristics mainly with the presence of high separated flows. Generally, the meanline design tools determine the flow properties at blade leading and trailing edges based on the Euler equations combined with loss models. This is not sufficient to account for the tri-dimensional effects of turbulence and the behavior of the flow in the blade annulus and blade-to-blade channel. CFD can be used as an important tool to check if the design values were in agreement with the engine requirements, as well as to improve the blade geometries aiming at high performance.

9. ACKNOWLEDGEMENTS

The authors would like to thank the Center for Reference on Gas Turbine at ITA for the support to this research work.

10. REFERENCES

- Adumitroaie, V., Ristorcelli, J.R. and Taulbee, D.B., 1998. *Progress in Favre-Reynolds Stress Closures for Compressible Flows*. NASA Contractor - CR-1998-2078423.
- Anderson, M., Gu, F. and MacLeod, P.D., 2003. "Application and Validation of CFD in a Turbomachinery Design System". In *ASME, IMECE2003-44217*.
- Casey, M., 1984. "Computational Methods for Preliminary Design and Geometry Definition in Turbomachinery". In *AGARD Lecture Series on Turbomachinery Design Using CFD*.
- Chen, J., Ghosh, A., Sreenivas, K. and Whitfield, D., 1997. "Comparison of Computations Using Navier-Stokes Equations in Rotating and Fixed Coordinates for Flow Through Turbomachinery". In *Aerospace Sciences Meeting & Exhibit - AIAA-97-0878*.
- Denton, J., 1990. "The Calculation of the Three Dimensional Viscous Flow Through Multistage Turbomachines". *ASME 90-GT-19*.
- Denton, J., 2010. "Some Limitations of Turbomachinery CFD". In *ASME Turbo Expo 2010, GT2010-22540*.
- Dunn, D.M., Zhou, D.W., Saha, K., Squires, K.D. and Roy, R.P., 2010. "Flow Field in a Single-Stage Model Air Turbine Rotor-Stator Cavity with Pre-Swirled Purge Flow". In *ASME Turbo-Expo 2010, GT2010-22869*.
- Fidalgo, V.J., Hall, C.A. and Colin, Y., 2010. "A Study of Fan-Distortion Interaction Within the NASA Rotor 67 Transonic Stage". In *ASME Turbo-Expo 2010, GT2010-22914*.
- Gmelin, C., Steager, M., Thiele, F., huppertz, A. and Swoboda, M., 2010. "Unsteady RANS Simulations of a Highly Loaded Low Aspect Ratio Compressor Stator Cascade with Active Flow Control". In *ASME Turbo-Expo 2010, GT2010-22516*.
- Grosvenor, A.D., 2007. "Rans Prediction of Transonic Compressive Rotor". In *ASME Turbo-Expo 2007, GT2007-37691*.
- Holmes, D.G., 1989. "Inviscid 2D Solutions on Unstructured, Adaptive Grids". Numerical Methods for Flows in Turbomachinery, VKI-LS 1989-06.
- Jameson, A., Schmidt, W. and Turkel, E., 1981. "Numerical Solutions of the Euler Equations by Finite Volume Methods Using Runge-Kutta Time-Stepping Schemes". In *Fluid and Plasma Dynamics Conference*.

- Lapworth, L. and Shahpar, S., 2004. "Design of Gas Turbine Engines Using CFD". *European Congress on Computational Methods in Applied Sciences and Engineering-ECOMAS 2004*.
- Mavriplis, D., 1990. "Accurate Multigrid Solution of the Euler Equations on Unstructured and Adaptive Meshes". *AIAA Journal*, Vol. 28, pp. 213–221.
- Richardson, G.A., Dawes, W.N. and Savill, A.M., 2006. "Cfd Analysis of Hot Gas Injection Mechanisms for the Vertical Descent Phase of a Harrier Aircraft". In *ASME Turbo-Expo 2006, GT2006-90766*.
- Soghe, R., Innocenti, L., Andreini, A. and Poncet, S., 2010. "Numerical Benchmark of Turbulence Modeling in Gas Turbine Rotor-Stator System". In *ASME Turbo-Expo 2010, GT2010-22627*.
- Spalart, P. and Allmaras, S., 1992. "A One-Equation Turbulence Model for Aerodynamic Flows". In *Aerospace Sciences Meeting & Exhibit, AIAA-92-0439*.
- Tomita, J.T., 2009. *Three-Dimensional Flow Calculations of Axial Compressors and Turbines Using CFD Techniques*. Ph.D. thesis, ITA, Sao Jose dos Campos, SP, Brazil.
- Veullot, J., 1985. "A 3D Euler Method for Internal Transonic Flows Computation with a Multi-Domain Approach". Technical Report TP n. 1985-51, ONERA, 29 Avenue de la Division Leclerc - 92320 CHATILLON.

11. Responsibility notice

The authors are the only responsible for the printed material included in this paper.